

Classification of Extremely Red Objects in the Hubble Ultra Deep Field

Guan-Wen Fang¹, Xu Kong^{1,2} and Min Wang¹

¹ Center for Astrophysics, University of Science and Technology of China, Hefei, Anhui, 230026, China;

² Joint Institute for Galaxy and Cosmology (JOINGC) of SHAO and USTC; xkong@ustc.edu.cn

Abstract In this paper we present a quantitative study of the classification of Extremely Red Objects (EROs). The analysis is based on the multi-band spatial- and ground-based observations (HST/ACS-*BVIz*, HST/NICMOS-*JH*, VLT-*JHK*) in the Hubble Ultra Deep Field (UDF). Over a total sky area of 5.50 arcmin² in the UDF, we select 24 EROs with the color criterion $(i - K)_{\text{Vega}} > 3.9$, corresponding to $(I - K)_{\text{Vega}} \gtrsim 4.0$, down to $K_{\text{Vega}} = 22$. We develop four methods to classify EROs into Old passively evolving Galaxies (OGs) and Dusty star-forming Galaxies (DGs), including $(i - K)$ vs. $(J - K)$ color diagram, spectral energy distribution fitting method, Spitzer MIPS 24 μm image matching, and nonparametric measure of galaxy morphology, and found that the classification results from these methods agree well. Using these four classification methods, we classify our EROs sample into 6 OGs and 8 DGs to $K_{\text{Vega}} < 20.5$, and 8 OGs and 16 DGs to $K_{\text{Vega}} < 22$, respectively. The fraction of DGs increases from 8/14 at $K_{\text{Vega}} < 20.5$ to 16/24 at $K_{\text{Vega}} < 22$. To study the morphology of galaxies with its wavelength, we measure the central concentration and the Gini coefficient for the 24 EROs in our sample in HST/ACS-*i, z* and HST/NICMOS-*J, H* bands. We find that the morphological parameters of galaxies in our sample depend on the wavelength of observation, which suggests that caution is necessary when comparing single wavelength band images of galaxies at a variety of redshifts.

Key words: galaxies: evolution — galaxies: fundamental parameters — galaxies: high-redshift — cosmology: observations

1 INTRODUCTION

Extremely Red Objects (EROs) are massive galaxies ($M_* > 10^{11} M_\odot$), characterized by extremely red optical-to-infrared colors and high redshifts (Hu & Ridgway 1994; Elston et al. 1988, 1989; Stern et al. 2006; Conselice et al. 2008a). EROs are now instead recognized to be primarily comprised of two interesting galaxy populations: **Old** passively evolving Galaxies (hereafter **OGs**) characterized by old stellar populations, and **Dusty** star-forming Galaxies (hereafter **DGs**) reddened by a large amount of dust. EROs continue to attract considerable interest, on the one hand, the research in the literature suggests that they may be the direct progenitors of present-day massive E/S0 galaxies. On the other hand, they can provide crucial constraints on the current galaxy formation and evolution models (Kitzbichler & White 2007). Therefore, the key question is then to measure the relative fraction of both galaxy types in order to exploit the stringent clues that EROs can place on the formation and evolution of elliptical galaxies and the abundance of dust obscured system at high redshift.

Many groups are currently investigating the fractions of these two ERO populations using a variety of observational approaches, but the fraction of OGs and DGs from different surveys is different. Some work found that OGs were dominant in EROs (Moriondo et al. 2000; Simpson et al. 2006; Conselice et al. 2008a), but the others reported nearly the opposite results, and found that most of EROs with spiral-like or irregular

morphology (Yan & Thompson. 2003; Cimatti et al. 2003; Sawicki et al. 2005). In addition, some authors also reported that the OGs and DGs have similar fractions in their EROs sample (e.g. Mannucci et al. 2002; Giavalisco et al. 2004; Moustakas et al. 2004). Therefore, one of the main open questions about EROs is the relative fraction of different ERO types.

To determine the relative fraction of different EROs accurately, we develop four methods for DGs and OGs classification, such as the $(i - K)$ vs. $(J - K)$ color diagram, the multi-wavelength spectral energy distribution (SED) fitting method, the Spitzer MIPS (Multiband Imaging Photometer for Spitzer) 24 μm image matching method, and the nonparametric measures of galaxy morphology method, including Gini coefficient (G), the second-order moment of the brightest 20% of the galaxy's flux (M_{20}), and rotational asymmetry (A) (Abraham et al. 1996, 2003; Bershadsky et al. 2000; Conselice 2003; Lotz et al. 2004, 2008; Conselice et al. 2008b). To check the reliability of these methods, for the first time, we applied our methods to the EROs sample over the Hubble Ultra Deep Field (hereafter UDF) in this paper. We will apply these methods for large data sets, such as GEMS and COSMOS in the future (Rix et al. 2004; Scoville et al. 2007).

We describe the multi-band spatial- and ground-based observations of the UDF; introduce data reduction and method for obtaining our EROs sample in Section 2. Section 3 presents the four classification methods of EROs and their application for EROs in the UDF. We present classification result and discuss the morphological parameters of EROs varying with wavelength in Section 4, and summarize our conclusions in Section 5. Throughout this paper, all magnitudes and colors are in the Vega system unless stated otherwise¹.

2 OBSERVATIONS, DATA REDUCTION AND EROS SELECTION

2.1 Observations

The UDF field lies within the *Chandra* Deep Field South (CDF-S, or Great Observatories Origins Deep Survey South, GOODS-S) with coordinates $\text{RA} = 03^{\text{h}}32^{\text{m}}39.0^{\text{s}}$, $\text{Dec} = -27^{\circ}47'29.1''$ (J2000) (Giavalisco et al. 2004; Beckwith et al. 2006). The field has been imaged by a large number of telescopes at a variety of wavelengths (Coe et al. 2006). In this paper, HST/ACS (Advanced Camera for Survey) images, HST/NICMOS (Near-Infrared Camera and Multi-Object Spectrometer) images, VLT/ISAAC (Infrared Spectrometer And Array Camera) images and a Spitzer/MIPS 24 μm image of the UDF were used.

With a total of 544 orbits, the UDF is one of the largest time allocations of HST, and indeed the filter coverage, depth, and exquisite quality of the UDF ACS and NICMOS images provide an unprecedented data set for the study of galaxy morphology, even of very low surface brightness components. They are taken in four optical bands and two near-infrared bands: $B(\text{F435W})$, $V(\text{F606W})$, $i(\text{F775W})$, $z(\text{F850LP})$, $J(\text{F110W})$ and $H(\text{F160W})$. Due to the small field of NICMOS camera, the UDF NICMOS only covers a subsection (5.76 arcmin^2) of the optical UDF (11.97 arcmin^2). For our analysis, we use the reduced UDF optical imaging data v1.0 made public by STScI on 2004 March 9. The 10σ limiting AB magnitudes are 28.7, 29.0, 29.0 and 28.4 for B -, V -, i - and z -band (Beckwith et al. 2006). The J - and H -band data are given by Thompson et al. (2005). The 5σ limiting AB magnitudes is 27.7 at 1.1 and 1.6 μm in a $0.6''$ diameter aperture.

In addition to the HST NICMOS and ACS data, we also use the Spitzer MIPS image. MIPS is one of the facilities on the Spitzer Space Telescope that is used to image at 24, 70 and 160 μm . In this paper, we use the super deep 24 μm image data only, which is part of the GOODS Spitzer Legacy Survey (PI: Mark Dickinson). GOODS/MIPS Data Release v3 was used for our analysis. In addition, ground-based near-infrared images (JHK) of the UDF are taken as part of the GOODS with VLT/ISAAC. GOODS/ISAAC Data Release v1.5 was used for our analysis. They are reduced using an improved version of the ESO/MVM image processing pipeline. The 5σ limiting AB magnitudes at J -, H - and K -band are 25.3, 24.8 and 24.4 in a $2.0''$ diameter aperture.

¹ The relevant conversion between AB and Vega magnitudes for this paper are $K_{\text{AB}} = K_{\text{Vega}} + 1.87$, $i_{\text{AB}} = i_{\text{Vega}} + 0.41$.

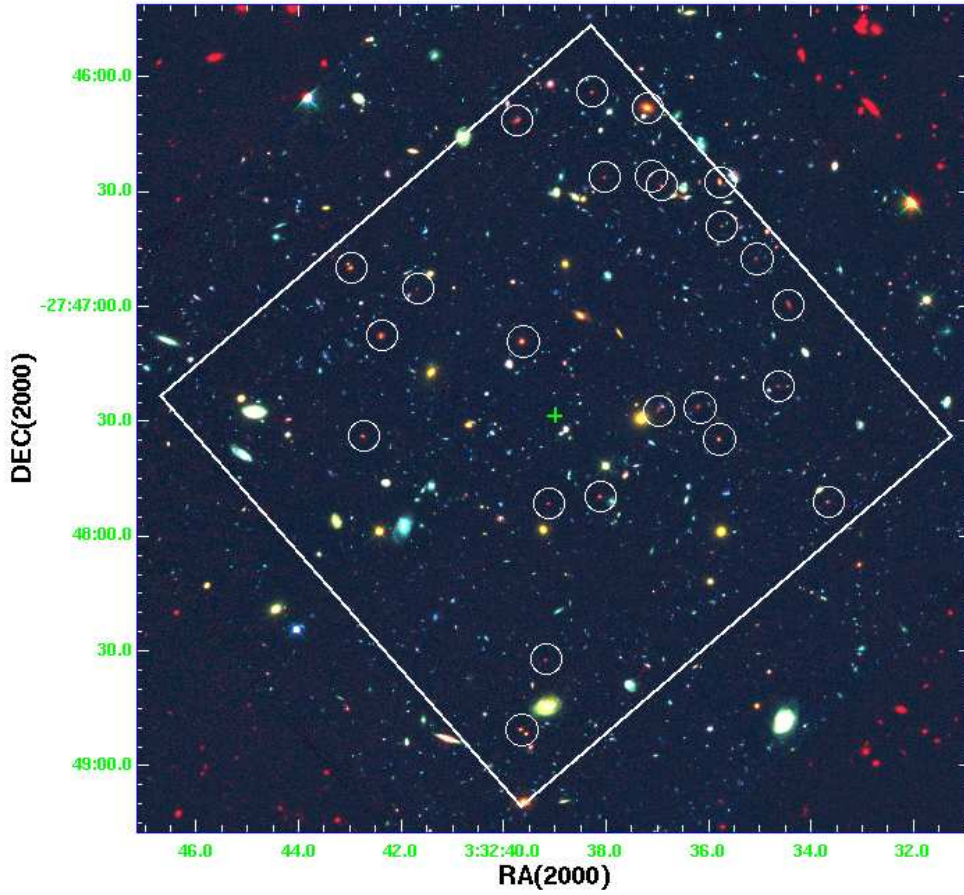


Fig. 1 Composite pseudo-color image of the UDF. The RGB colors are assigned to VLT-*K*, ACS-*z*, and ACS-*B* band images. The outlined (white) region of the image is the field where the NICMOS-*JH* band images have a high signal-to-noise ratio (5.5 arcmin²). The small white circles show the sky positions of 24 EROs in the UDF.

2.2 Data reduction

All of these data have been released in fully processed form and no additional processing is necessary. However, considering that the images in different data sets have different scales and sizes, so they must be resampled to put them on the same astrometric grid. The resampling was done with IRAF's *geomap* and *geotran* tasks. All images were remapped to $0.09'' \text{ pixel}^{-1}$, the same scale as the NICMOS *J*-band and *H*-band images. By comparing the resampled images around the galaxy luminosity, we found that the resampling process of the sample could not cause each source deviation in the position or the flux. In addition, the edges of the HST/NICMOS images have only one integration, as compared to the average 16 integrations for the interior of the images. Therefore, the edges of the resulting final images, where the signal-to-noise of HST/NICMOS images was very low, were then trimmed. Figure 1 shows a composite pseudo-color image of the UDF. The area, as discussed in this paper, was reduced from HST/NICMOS's 5.76 to 5.50 arcmin², as the white outlined region of the image.

Source extraction in the science image was performed with the program SExtractor version 2.5 (Bertin & Arnout, 1996) in the dual image mode, a $2''$ diameter aperture was used for aperture magnitudes. More detailed description about catalog construction can be found in Kong et al. (2008a). Compared to the optical selection, the near-infrared selection has several advantages, in particular in the K-band (Broadhurst

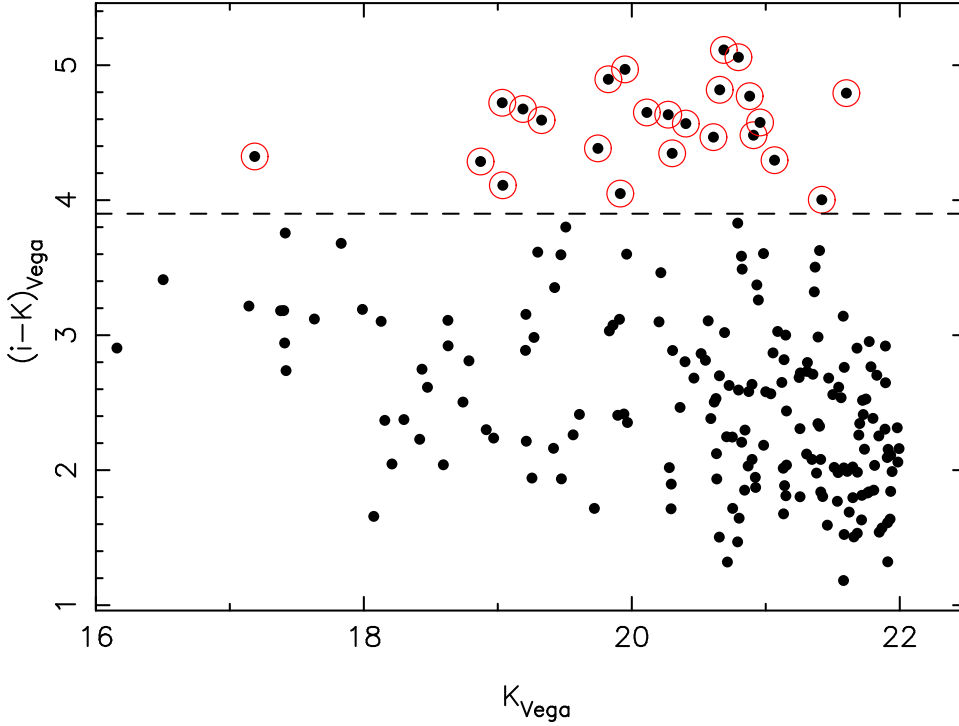


Fig. 2 K -band magnitude vs. $(i - K)$. All galaxies in the K -limited sample in the UDF are plotted as filled circles, and EROs are overlaid with larger open circles. The dashed line shows the threshold of $(i - K) = 3.9$ for selecting EROs.

et al. 1992; Kauffmann & Charlot. 1998). Therefore, we select objects to $K < 22$ over a total sky area of 5.5 arcmin^2 in the UDF, and 210 objects (including 202 galaxies and 8 stars, star-galaxy separation using the same method as that in Kong et al. 2006) were included in our final catalog. A comparison of the K -band number counts in the UDF survey with a compilation of counts published in the literature can be found in the figure 2 of Kong et al. (2008a). The red-, black-, green- and blue-filled squares correspond to the counts of field galaxies in the UDF (this paper), COSMOS (Kong et al. 2008b), Daddi-F and Deep3a-F (Kong et al. 2006), respectively. As shown in that figure, our number counts in different fields are in good agreement with those of the previous surveys.

2.3 ERO Sample Selection

Numerous different selection criteria have been defined for EROs, including $R - K \geq 6$, $R - K \geq 5.3$, $R - K \geq 5$, $I - K \geq 4$ in the Vega magnitude system with K -magnitude upper limits from 18 to 20, or $R - [3.6] \geq 4$ in the AB magnitude system (e.g. Hu & Ridgway. 1994; Scodeggio & Silva. 2000; Brown et al. 2005; Kong et al. 2006; Díaz-Sánchez et al. 2007; Wilson et al. 2007). Since the UDF field has not I -band or R -band observation data, we cannot use $R - K$ or $I - K$ color criteria for EROs selection. In this paper, we use ACS- i and ISAAC- K for EROs selection. We calculated $i - K$ color using SEDs from the Kodama & Arimoto (1997, KA97)'s library, and found $(i - K) > 3.9$ can be used to select both ellipticals and reddened starbursts when their redshift is beyond 0.8. Therefore, EROs in this paper are selected by $(i - K) > 3.9$, which corresponds to $(I - K) > 4$. $2''$ diameter aperture magnitudes were used for color calculation.

Figure 2 shows the color-magnitude plot for all 202 galaxies, with $K < 22$, in the UDF. 24 galaxies with $(i - K) > 3.9$ were selected as EROs, and they are plotted in Figure 2 as larger circles, for a surface

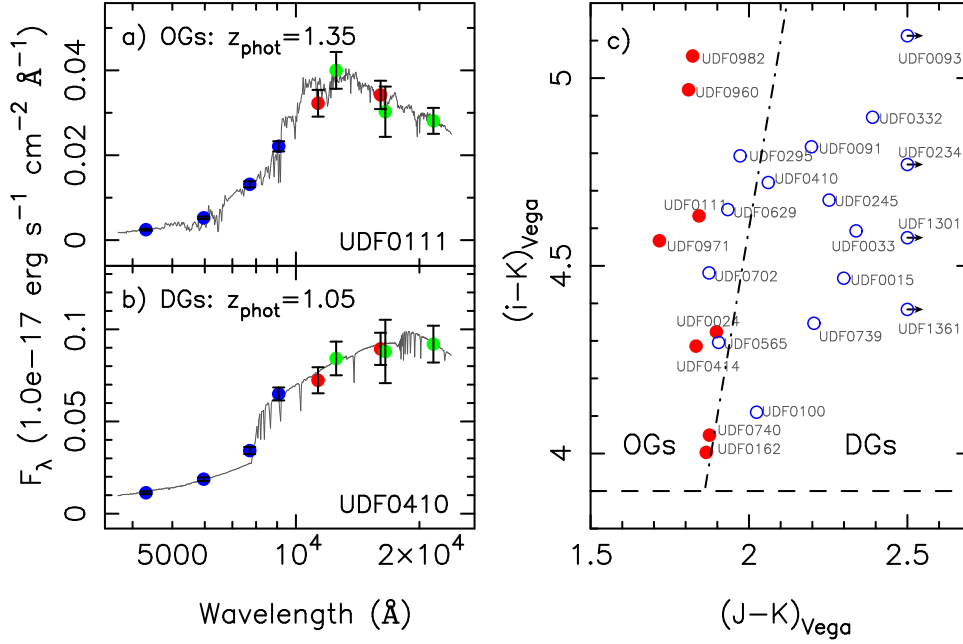


Fig. 3 Left panel: Spectral energy distribution of two EROs in the UDF. Filled circles show the observed photometric data, and solid curves show the best fitting templates. Photometric redshift and name for each ERO are shown also. Blue, red and green colors are assigned to ACS- $BViz$, NICMOS- JH and VLT- JHK bands, respectively. Right panel: Distribution of EROs on $(i-K)$ versus $(J-K)$ diagram. EROs classified as OGs by the SED fitting method are plotted in red filled circles, and as those DGs are plotted as blue open circles. The dashed line correspond to the threshold of $(i-K) = 3.9$ for selecting EROs in this paper, the dot-dashed line is a new color criterion for EROs classification, based on evolutionary population synthesis model (see the next subsection for detail).

density of 4.36 arcmin^{-2} to $K < 22$. The K -band differential number counts of EROs in the UDF are plotted in the figure 2 of Kong et al. (2008a) also, as those of field galaxies. We found that the differential number counts of EROs in different fields are in good agreement. In addition, the slope of the number counts of EROs is a variable, being steeper at bright magnitudes and flattening out towards faint magnitudes. A break in the counts is present at $K \sim 18$, very similar to the break in the ERO number counts observed by previous works.

3 CLASSIFICATION OF EROS

Many researchers have attempted to separate the two types of EROs by various methods. However, their results conflict with each other. In order to estimate the relative fraction of OGs and DGs in EROs, we develop four classification methods, and try to apply them to the ERO sample of the UDF in this section.

3.1 Classification based on SED Fitting

An SED fitting technique based on the photometric redshift code *HyperZ* (Bolzonella et al. 2000) is used to classify our ERO sample into different types, dusty and evolved, using their multi-waveband photometric properties. The efficiency of the method is based on the fit of the overall shape of the spectra and the detection of strong spectral features, such as the 4000\AA break, the Balmer break, or strong emission lines (Smail et al. 2002; Miyazaki et al. 2003; Georgakakis et al. 2008; Stutz et al. 2008).

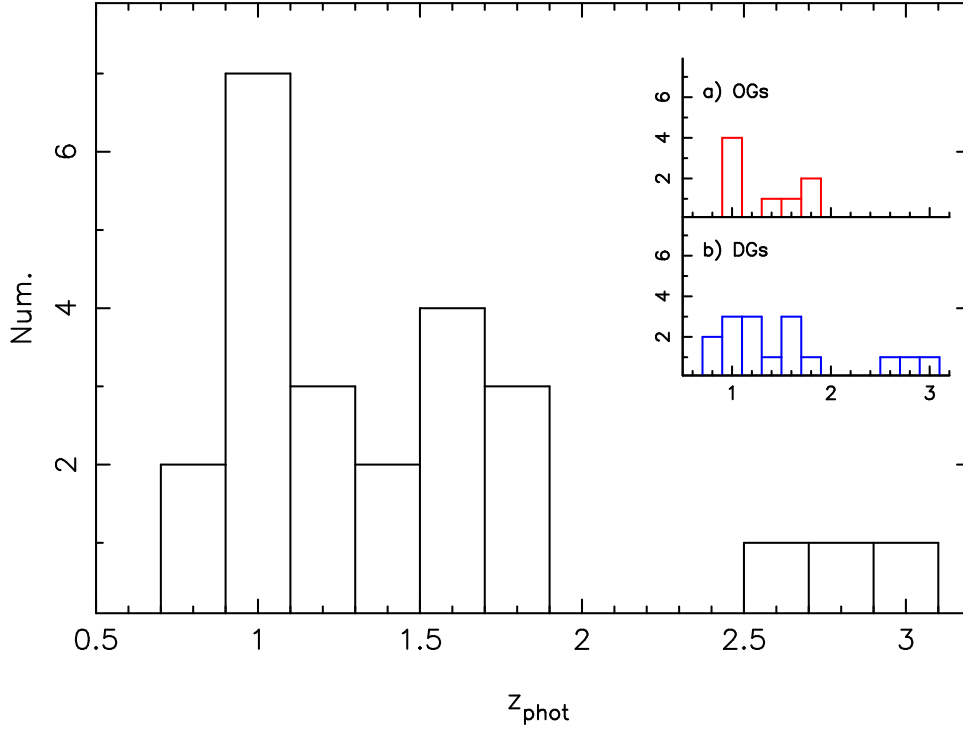


Fig. 4 Photometric redshift distribution of EROs in the UDF. Panel a) shows the redshift distribution of OGs, and Panel b) shows the redshift distribution of DGs.

To illustrate this point more clearly, we show the SEDs of 2 EROs, as an example, in the left panel of Figure 3. The blue-, red-, and green-filled circles correspond to the observed data of ACS-*BViz*, NICMOS-*JH* and ISAAC-*JHK* bands, respectively. The best fitting SEDs of these two galaxies using the photometric redshift technique are shown as grey lines. The upper-panel represents typical OGs, and the lower panel represents a typical DGs. From this figure, we can find that OGs shows a large break at 4000Å rest-frame and the flux decreases at near-infrared band; DGs shows a small 4000Å break, a flat SED at optical and near-infrared rest-frame wavelength, because of dust extinction and dust radiation. As a result, we can use the SED fitting method to classify EROs into OGs and DGs.

We use a stellar population synthesis model by KA97 to make template SEDs, similar to Miyazaki et al. (2003). KA97 includes the chemical evolution of gas and stellar populations, and have been successfully used to obtain photometric redshifts of high and low redshift galaxies (Kodama et al. 1999, Furusawa et al. 2000). The template SEDs consist of the spectra of pure disks, pure bulges, and intermediate SED types. Pure disk SEDs correspond to young or active star-forming galaxies, and pure bulge SEDs correspond to elliptical galaxies. The intermediate SED types (composites) are made by combining a pure bulge-like spectrum and a pure disk-like spectrum, the ratio of the bulge luminosity to the total luminosity in the *B* band is changed from 0.1 to 0.99. Full details of the templates can be found in Furusawa et al. (2000) and Kong et al. (2008b). The SED derived from the observed magnitudes of each object, including ACS-*BViz*, NICMOS-*JH*, and ISAAC-*JHK*, is compared to each template spectrum (redshift from 0.0 to 5.0 with step 0.05; A_V from 0.0 to 6.0 with step 0.05; internal reddening law introduced by Calzetti et al. 2000) in turn. Figure 3 in Kong et al. (2008a) shows a comparison of the photometric redshifts from our SED fitting method with their spectroscopic redshifts for 33 galaxies in the UDF. From that figure, we found that our photometric redshifts fit the spectroscopic redshifts well, with an average $\delta z / (1 + z_{\text{spec}}) = 0.02$.

Figure 4 shows the photometric redshift histogram of EROs in our sample. The peak of the redshift distribution is at $z_{\text{phot}} \sim 1.0$, all of them have $z_{\text{phot}} > 0.8$. Only 3 EROs have redshift $z_{\text{phot}} > 2.0$, those

Table 1 Properties, Nonparametric Morphological Indicators and Classification of EROs in the UDF.

NAME (1)	RA (2)	DEC (3)	K_{tot} (4)	$i-K$ (5)	$J-K$ (6)	A_V (7)	z_{phot} (8)	C (9)	A (10)	G (11)	M_{20} (12)	M1 (13)	M2 (14)	M3 (15)	M4 (16)	End (17)
UDF0015	53.1593971	-27.7677822	20.61	4.47	2.30	0.95	1.04	0.36	0.035	0.53	-1.450	DG	DG	DG	DG	DG
UDF0024	53.1549187	-27.7689114	17.18	4.32	1.90	0.10	1.04	0.58	0.023	0.68	-2.197	OG	OG	OG	OG	OG
UDF0033	53.1655121	-27.7698059	19.33	4.59	2.34	1.00	1.45	0.33	0.172	0.50	-1.725	DG	DG	DG	DG	DG
UDF0091	53.1546974	-27.7738743	20.66	4.82	2.20	1.15	0.84	0.17	0.010	0.37	-0.842	DG	DG	OG	DG	DG
UDF0093	53.1583939	-27.7739716	20.69	5.11	2.68	2.20	1.80	0.41	0.128	0.56	-1.738	DG	DG	DG	DG	DG
UDF0100	53.1490250	-27.7743092	19.04	4.11	2.02	2.85	0.92	0.31	0.121	0.52	-1.361	DG	DG	DG	DG	DG
UDF0111	53.1537590	-27.7745819	20.27	4.63	1.84	0.15	1.35	0.49	0.019	0.65	-1.657	OG	OG	OG	OG	OG
UDF0162	53.1488419	-27.7775211	21.42	4.00	1.87	0.80	1.82	0.52	0.122	0.68	-1.413	OG	OG	DG	OG	OG
UDF0234	53.1460953	-27.7798824	20.88	4.77	3.38	1.70	2.72	0.33	0.111	0.46	-1.516	DG	DG	DG	DG	DG
UDF0245	53.1790085	-27.7805386	19.19	4.68	2.25	1.30	0.89	0.37	0.171	0.55	-1.364	DG	DG	DG	DG	DG
UDF0295	53.1736145	-27.7820663	21.60	4.79	1.77	0.80	1.56	0.21	0.029	0.40	-0.607	DG	OG	DG	DG	DG
UDF0332	53.1434212	-27.7832375	19.83	4.90	2.39	2.00	1.14	0.18	0.077	0.41	-0.406	DG	DG	DG	DG	DG
UDF0410	53.1765213	-27.7854481	19.03	4.72	2.06	0.75	1.05	0.31	0.112	0.54	-1.172	DG	DG	DG	DG	DG
UDF0414	53.1651039	-27.7858753	18.87	4.29	1.83	0.55	0.94	0.45	0.054	0.60	-1.920	OG	OG	OG	OG	OG
UDF0565	53.1442566	-27.7891445	21.07	4.30	1.90	1.25	1.15	0.21	0.085	0.47	-1.163	DG	OG	DG	DG	DG
UDF0629	53.1507835	-27.7906094	20.11	4.65	1.93	3.60	1.51	0.38	0.082	0.58	-1.620	DG	OG	OG	DG	DG
UDF0702	53.1539879	-27.7908936	20.91	4.48	1.87	2.90	1.63	0.23	0.108	0.43	-1.145	DG	OG	DG	DG	DG
UDF0739	53.1780281	-27.7927475	20.30	4.35	2.21	1.05	1.24	0.14	0.148	0.32	-1.044	DG	DG	DG	DG	DG
UDF0740	53.1491013	-27.7929821	19.91	4.05	1.88	0.50	1.09	0.50	0.064	0.64	-1.806	OG	OG	OG	OG	OG
UDF0960	53.1587563	-27.7971535	19.95	4.97	1.81	0.05	0.93	0.49	0.030	0.68	-1.542	OG	OG	OG	OG	OG
UDF0971	53.1402855	-27.7975273	20.40	4.57	1.72	0.80	1.50	0.50	0.077	0.64	-1.749	OG	OG	OG	OG	OG
UDF0982	53.1629448	-27.7976551	20.80	5.06	1.82	0.25	1.90	0.36	0.067	0.60	-1.424	OG	OG	OG	OG	OG
UDF1301	53.1631813	-27.8089867	20.96	4.58	3.35	1.70	2.63	0.31	0.077	0.58	-1.362	DG	DG	OG	DG	DG
UDF1361	53.1652374	-27.8140640	19.75	4.38	3.14	2.15	2.90	0.57	0.153	0.70	-1.824	DG	DG	DG	OG	DG

Note. — Column (4): K -band total magnitude in Vega; Columns (5) – (6): the color of $i - K$ and $J - K$ in Vega; Columns (7) – (8): the dust extinction and photometric redshifts of EROs; Columns (13) – (16): classification results of EROs with different method, M1 from the SED fitting method, M2 from the $(i - K)$ vs. $(J - K)$ color diagram, M3 from the MIPS $24 \mu\text{m}$ image, M4 from the nonparametric morphological indicators; Column (17): the final classification results, considering the results of M1, M2, M3, and M4.

are faint dusty EROs. The small panels in Figure 4 show the redshift distribution of OGs (in panel a) and DGs (in panel b). It is worth noting that OGs have a narrow redshift distribution, none of them have redshift higher than 2.0. Photometric redshifts (z_{phot}) and absorption in the V band (A_V) of EROs are listed in Table 1 also.

Based on this SED fitting method, we classify EROs as DGs, if the best fitting template of it is the spectra of disk-dominant (late type SEDs); the others were classified as OGs (early type SEDs). Out of the 24 EROs in our sample, 8 are classified as OGs, while 16 are classified as DGs. The results are listed in Table 1. Column (1) lists the galaxy name. Columns (2) and (3) list the right ascension and declination at epoch 2000; units of right ascension and declination are degree. Column (4) lists K -band total magnitude in the Vega system; Columns (5) and (6) list the color of $i - K$ and $J - K$ in the Vega magnitude. Columns (7) and (8) list the dust extinction (A_V) and photometric redshift (z_{phot}) for each source. Columns (9) – (12) list the morphological parameters of concentration index (C), Gini coefficient, M_{20} , and rotational asymmetry (see Section 3.4). Column (13) lists the classification results of EROs with the SED fitting method (M1, the first classification method in this paper).

In the right panel of Figure 3, EROs in the UDF were plotted in the $(i - K)$ vs. $(J - K)$ color diagram. The dashed line corresponds to the threshold of $(i - K) = 3.9$ for selecting EROs in this paper, the dot-dashed line is a new color criterion for EROs classification, based on evolutionary population synthesis model (see the next subsection for detail). OGs, classified by the SED fitting method, were plotted in red filled circles; DGs were plotted as blue open circles. We found all OGs stayed at the left space of the dot-dashed line, most (12/16) of DGs stayed at the right space of the dot-dashed line.

3.2 Classification based on $(i - K)$ vs. $(J - K)$ Diagram

Pozzetti & Mannucci. (2000) have introduced a method to classify EROs into OGs and DGs based on their locations in the $(I - K)$ vs. $(J - K)$ plane. EROs with $(J - K) > 0.36(I - K) + 0.46$ were classified as DGs, and the others are OGs. This method makes the $(I - K)$ vs. $(J - K)$ plane use a characteristic difference in the spectra of OGs and DGs located at $0.8 < z < 2$; OGs have a steep drop shortward of 4000 Å, while DGs' spectra are smoother, giving DGs' $J - K$ colors redder than OGs. As a consequence, OGs are located at the left part of the $(I - K)$ vs. $(J - K)$ color diagram, while DGs are located at the right part.

To classify the EROs in our sample, and check the validity of our SED fitting method, we apply the color-color method to our sample also. Because the i -band (F775W) filter in the UDF is different from the I -band filter used by Pozzetti & Mannucci. (2000), we have to develop our color criterion for EROs classification. Figure 5 shows $(i - K)$ vs. $(J - K)$ model color-color diagram of several representative galaxies with redshift $0.8 < z < 2.5$. Model SEDs are adopted from the KA97 library, the lines represent elliptical galaxies (pure bulge) with an extinction of $E(B - V) = 0.0$ (dotted), starburst galaxies (pure disk) with $E(B - V) = 0.5$ (dashed), and starburst galaxies with $E(B - V) = 0.7$ (dot-dashed), respectively. From this figure, we found the color criterion $(J - K) = 0.20(i - K) + 1.08$ (thick dot-dashed line) can be used to separate OGs and DGs for $0.8 < z < 2.5$. Using this new color criterion, we classified our EROs as OGs, if their $(J - K) < 0.20(i - K) + 1.08$. The others were classified as DGs. The classification results based on the $(i - K)$ vs. $(J - K)$ color-color diagram are listed in the 14th column (M2, the second classification method) of Table 1.

In Figure 5, EROs are plotted as filled (OGs) and open circles (DGs), respectively, classified by the SED fitting method. We found 12 EROs in the dusty starburst side, and the other 12 EROs fell on the elliptical side of the division. The agreement between the SED fitting method and the $(I - K)$ vs. $(J - K)$ color diagram is found to be satisfactory. All EROs classified as OGs by the SED fitting method are also regarded as OGs by the $(i - K)$ vs. $(J - K)$ method. Similarly, 12 out of the 16 EROs which are classified as DGs by the SED fitting method are located at the dusty starburst side. There are 4 EROs (UDF0295, UDF0565, UDF0629 and UDF0702) which are classified as DGs by the SED fitting method, but are located at the left-hand side of the thick dot-dashed line. These galaxies are all close to the dividing line and very faint in K -band, the photometric uncertainty of those faint EROs may cause this discrepancy.

3.3 Classification based on Spitzer MIPS 24 μm Image

Old stellar populations show a turn-down at wavelengths longer than the rest-frame 1.6 μm "bump", while dusty starburst populations show emission from small hot dust grains and 6-12 μm polycyclic aromatic hydrocarbon (PAH) features. Therefore, the difference of ellipticals and dusty starbursting galaxies is very large at mid-infrared, dusty EROs should have strong mid-infrared flux. Between $z \sim 1 - 2$, rest-frame 6-12 μm PAH and dust features redshift into the 24 μm band. Any EROs detected at 24 μm images should belong to the dusty population. Therefore, Spitzer MIPS 24 μm data can be used to help us distinguish among different ERO populations (Rieke et al. 2004; Werner et al. 2004; Yan et al. 2004; Shi et al. 2006).

A detailed description of the GOODS-S MIPS 24 μm observations, data reductions, and data products can be found on Data Release 3 webpage. Source extraction at 24 μm was carried out using prior positional information determined from the very deep IRAC 3.6 and 4.5 μm images, with a flux limit $\geq 80 \mu\text{Jy}$. To merge our ERO sample and the MIPS 24 μm source catalog, we used a simple positional matching method with a 2.4'' match diameter, which corresponds to a 3σ combined astrometric uncertainty from the K -band and 24 μm data. However, of the 24 EROs in the UDF, only 6 galaxies have 24 μm emission with flux greater than 80 μJy . We plotted these 6 EROs on the MIPS 24 μm image with crosses (cyan) in Figure 6.

To check the reason for this low fraction of 24 μm -detected EROs, we plotted all 24 EROs in the UDF on the MIPS 24 μm image in Fig. 6. EROs are plotted as red (OGs) and blue (DGs) circles, respectively, classified by the SED fitting method. We found that, beside these six 24 μm bright EROs, the other 8 EROs have counterparts in MIPS 24 μm image also. The reason that these 8 EROs can not be found in the MIPS 24 μm catalog is that the flux limit of the catalog, 80 μJy , is too high for faint EROs. We classify these 6 + 8 EROs as DGs, and list them in the 15th column (M3, the third classification method) of Table 1, the others as OGs by this method. For the 16 EROs in the UDF, which were classified as DGs by the SED fitting

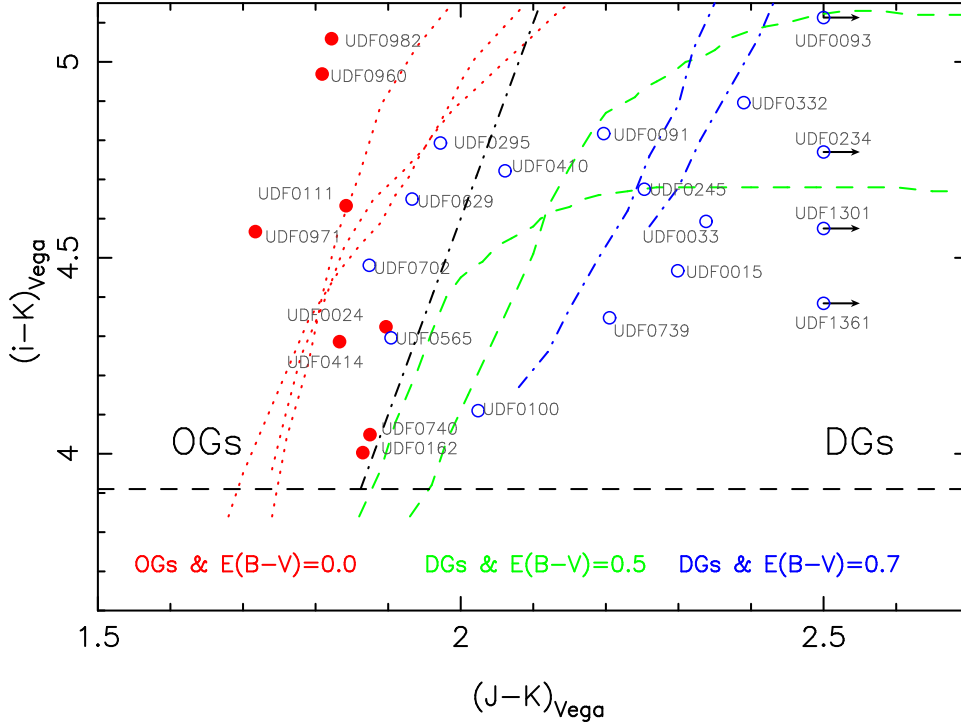


Fig. 5 $(i - K)$ plotted against $(J - K)$ for 24 EROs in the UDF. The dotted (elliptical galaxies with $E(B - V) = 0.0$, OGs), dashed (starburst galaxies with $E(B - V) = 0.5$) and dot-dashed (starburst galaxies with $E(B - V) = 0.7$) lines show color evolution of several representative model templates, using KA97 models. The lines are plotted up to redshift of $z = 2.5$. The thick dot-dashed line, $(J - K) = 0.20(i - K) + 1.08$, corresponds to the boundary for separation of OGs and DGs using $i - K$ vs. $J - K$ color. The horizontal line and the data points are the same as in Fig. 3.

method, 13 of them have counterparts on the the MIPS 24 μm image; the left 3 EROs (UDF0091, UDF0629 and UDF1301) do not have counterparts, and are very faint in K -band. For the 8 EROs in the UDF, which were classified as OGs by the SED fitting method, only one of them (UDF0162) has a counterpart on the MIPS 24 μm image, but the distribution of 24 μm radiation around this ERO is very diffuse.

3.4 Classification based on Galaxy Morphology

Figure 7 shows the color images for 24 EROs in the UDF, in which HST/ACS z -band, i -band and V -band were used as red, green and blue color. These images have high spatial resolution ($0.03'' \text{ pixel}^{-1}$), most of them show clear two dimensional structures. To classify EROs as OGs or DGs, we have measured four morphological parameters, Gini coefficient (the relative distribution of the galaxy pixel flux values, or G), M_{20} (the second-order moment of the brightest 20% of the galaxy's flux), concentration index (C) and rotational asymmetry index (A) for the EROs in our sample, with the high resolution ($0.03'' \text{ pixel}^{-1}$) ACS- i (F775W) images, and listed them in Table 1.

The left panel of Figure 8 shows the distribution of 24 EROs (filled and open circles represent OGs and DGs, classified by the SED fitting method) in the $\log G$ versus M_{20} plane. The distribution of EROs is very similar to that of local galaxies in Lotz et al. (2004), with OGs showing high G and low M_{20} values, and DGs with lower G and higher M_{20} values. The solid line is defined as $M_{20} = 15 \log G + 1.85$, and the

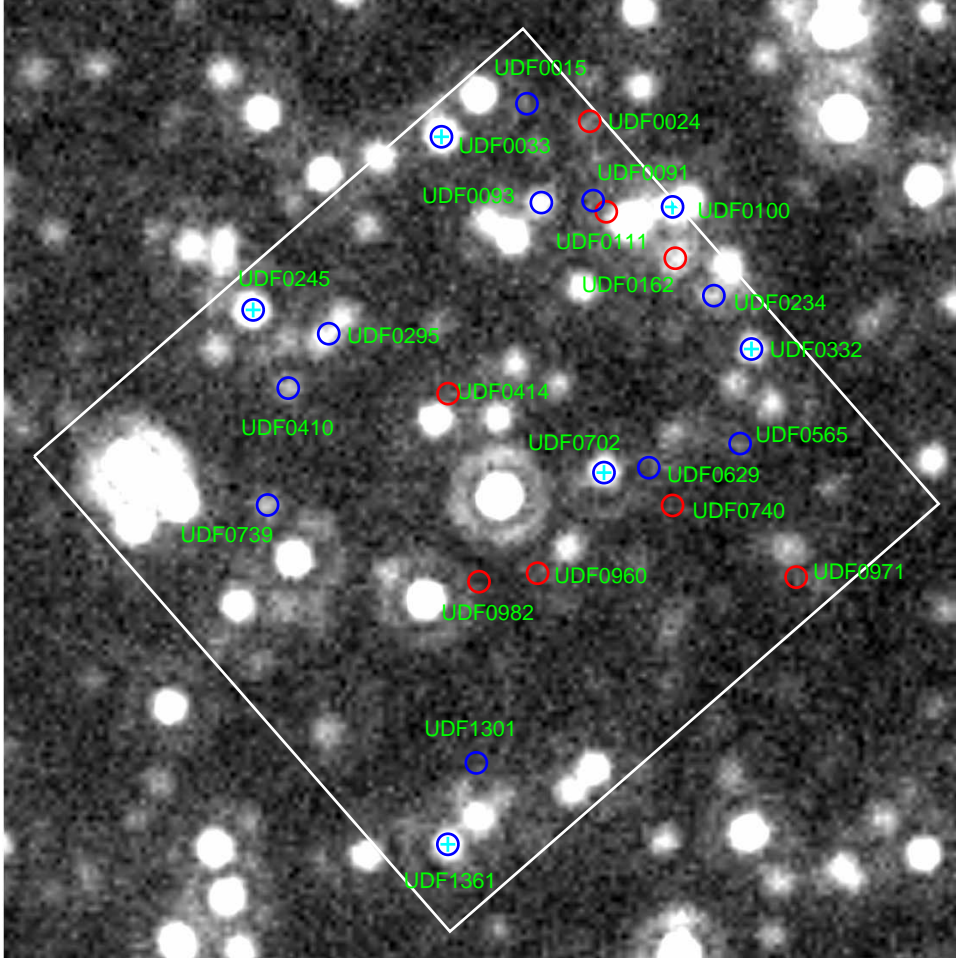


Fig. 6 Distribution of the 24 EROs in the UDF on the Spitzer MIPS 24 μm image. Red circles and blue circles represent OGs and DGs, respectively, classified by the SED fitting method. The size of circle is in 2.4'' diameter. EROs with $f_{24} > 80 \mu\text{Jy}$ are plotted as cyan crosses. The white outline is same as in Fig 1.

dot-dashed line is defined as $\log G = -0.23$. Both of these lines can be used to separate OGs and DGs, galaxies on the left side of them are DGs, while on the right side are OGs, except for UDF1361.

The right panel of Figure 8 shows the distribution of EROs in the $\log G$ versus $\log A$ plane. As found in Capak et al. (2007) for local galaxies, late type galaxies have lower G and higher A values, early type galaxies have higher G and lower A values. The solid line is defined as $\log A = 7.0 \log G + 0.4$, can also be used to classify late type and early type galaxies in our sample, except for UDF1361. As for UDF1361, it was classified as a DG by the former three classification methods, however, it was classified as OG by the morphology classification method. After checking its image in Figure 7, we found that one of the possible reason is that the nonparametric classification method can not separate ellipticals and early spiral galaxies with a big bulge, it may also be because of recent or on-going merges and interaction of this galaxy.

Since the Gini coefficient has a very strong correlation with the central concentration (C) for EROs in our sample, and the relationship between $C - A$, $C - M_{20}$ are similar to those of $G - A$, $G - M_{20}$, we do not plot these diagrams in this paper. As a conclusion, we found that OGs have higher G and lower M_{20} , A , but DGs have lower G and higher M_{20} , A ; all of these structural indices are efficient for separating

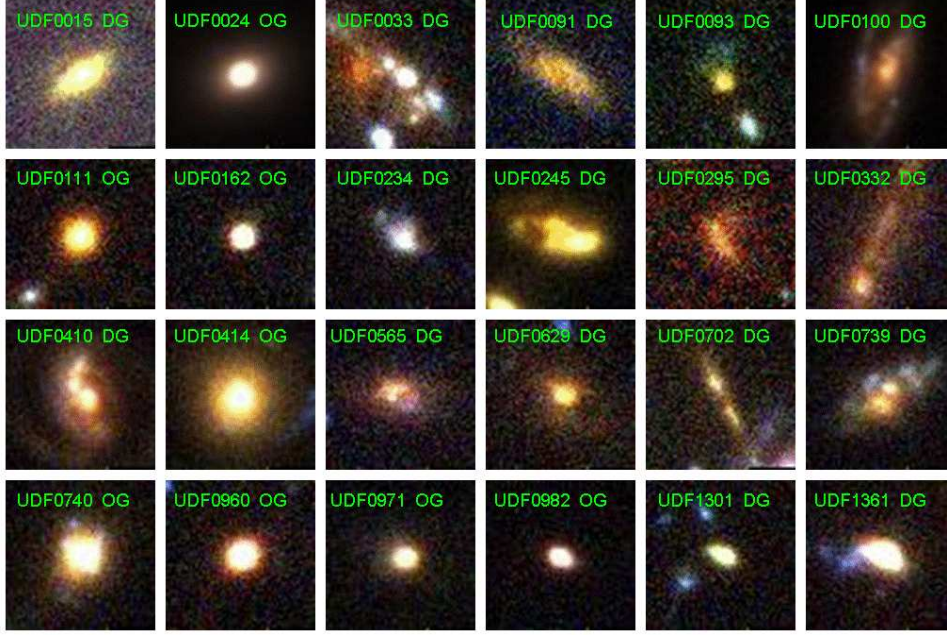


Fig. 7 Color composite images of 24 EROs in the UDF. Red represents the ACS- z filter, green represents the ACS- i filter, and blue represents the ACS- V filter. The regions shown are 1.8×1.8 arcsec² in size, and north is down, east to the right. Names and classification are displayed in upper right corners. The classification here is based on the final classification results, considering the results of M1, M2, M3, M4.

OGs and DGs; the classification results (9 OGs and 15 DGs) are listed in the 16th column (M4, the fourth classification method) of Table 1. The classification of EROs, using morphological parameters, are in good agreement with the result based on the SED fitting method.

4 RESULTS AND DISCUSSION

4.1 Results

As described in Section 3, we have developed four different methods to classify EROs into old passively evolving galaxies and dusty star-forming galaxies. From Columns (13) – (16) of Table 1, we found that the agreement among these different methods is found to be satisfactory. For those 24 EROs in the UDF, 16 of them are classified as the same ERO type (7 OGs and 9 DGs) by these different methods. However, for the other 8 EROs in our sample, they may be classified as OGs by one method, and while they may be classified as DGs by the other methods.

For these four classification methods, the $(i - K)$ versus $(J - K)$ color-color diagram is simple, however, it depends on reddening, redshift, and photometric accuracy. Therefore, it is difficult to separate some objects of both classes fall near the discriminating line between starburst and elliptical. For 4 EROs (UDF0295, UDF0565, UDF0629 and UDF0702) in our sample, which are classified as DGs by the other 3 methods, but are located at the left-hand side of the discriminating line, and classified as OGs by the $(i - K)$ versus $(J - K)$ method. Considering these EROs are close to the dividing line and faint, the photometric uncertainty of them may cause this discrepancy. We classified them as OGs.

The Spitzer MIPS 24 μ m image can help us to distinguish DGs accurately, by finding their counterparts in the mid-infrared band. However, due to the low spatial resolution of the Spitzer-MIPS instrument and low detection threshold, this method can not be used for very faint EROs. The classification results for the

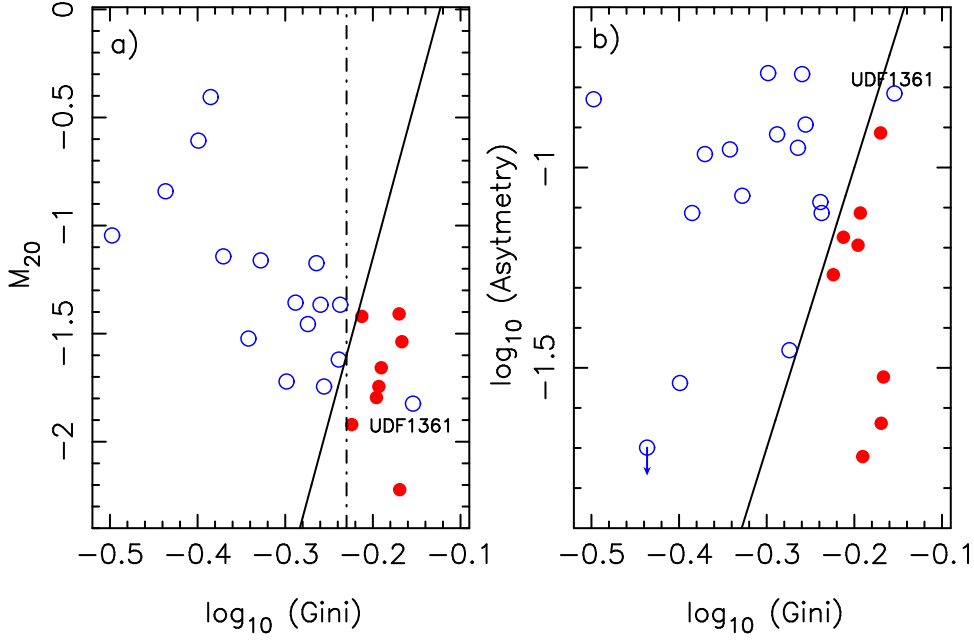


Fig. 8 a) M_{20} versus Gini coefficient for EROs in the UDF. The solid line is defined as $M_{20} = 15 \log G + 1.85$, and the dot-dashed line is defined as $\log G = -0.23$. b) Asymmetries versus Gini coefficient. The solid line is defined as $\log A = 7.0 \log G + 0.4$. Filled- and open-circles represent OGs and DGs, respectively, classified by the SED fitting method.

3 faint EROs (UDF0091, UDF0162, and UDF1031) by this method are different from the other 3 methods. We classify these 3 EROs into OGs and DGs based on the other 3 methods.

The SED fitting method and the nonparametric measures of galaxy morphology method almost offer the same result for EROs classification, except for UDF1361. UDF1361 was classified as DGs by the SED fitting method, the $(i - K)$ versus $(J - K)$ diagram, and the Spitzer MIPS $24 \mu\text{m}$ image method, but the nonparametric measures of galaxy morphology method classified it as OGs. This EROs has late type SEDs, but elliptical type morphologies. We classify it as DGs.

We finally divide our EROs sample into 8 OGs and 16 DGs, corresponding to 33% and 67% of the whole sample. The detailed results are shown in the last column of Table 1. Although our sample is small, this ratio is consistent with the fractions given by previous works (Yan & Thompson. 2003; Cimatti et al. 2003; Sawicki et al. 2005). In other words, most of EROs (down to $K = 22$) in our sample are DGs, which have spiral-like or irregular morphology.

4.2 Discussion

Galaxy morphology correlates with a range of physical properties in galaxies, such as mass, luminosity, and, particularly, color, and this suggests that morphology is crucial in our understanding of the formation and evolution of galaxies (Li et al. 2007). Moreover, the growing acceptance of the notion that galaxy morphology evolves continuously throughout a galaxy's lifetime. However, because of band-shifting effects, when we study the redshift evolution of galaxy morphology, we have to use different rest-frame wavelength images for comparison (for example, galaxies in the COSMOS field have high spatial resolution images at HST/ACS F814W-band only).

To investigate the galaxy morphology as a function of wavelength, we have measured the central concentration and the Gini coefficient for 24 EROs in the UDF, using the deep and high spatial resolution HST/ACS- iz ($0.03'' \text{ pixel}^{-1}$) and HST/NICMOS- JH ($0.09'' \text{ pixel}^{-1}$) band images. The results are listed

Table 2 Gini coefficient and concentration index at HST/ACS *i*-band (F775W), *z*-band (F850LP), HST/NICMOS *J*-band (F110W) and *H*-band (F160W) for the 24 EROs in the UDF.

NAME (1)	<i>G</i> (F775W) (2)	<i>C</i> (F775W) (3)	<i>G</i> (F850LP) (4)	<i>C</i> (F850LP) (5)	<i>G</i> (F110W) (6)	<i>C</i> (F110W) (7)	<i>G</i> (F160W) (8)	<i>C</i> (F160W) (9)
OGs								
UDF0024	0.677	0.576	0.680	0.581	0.700	0.562	0.703	0.590
UDF0111	0.645	0.491	0.662	0.458	0.653	0.492	0.698	0.527
UDF0162	0.676	0.524	0.646	0.479	0.498	0.346	0.508	0.350
UDF0414	0.597	0.449	0.614	0.460	0.640	0.504	0.695	0.565
UDF0740	0.637	0.497	0.664	0.504	0.653	0.484	0.715	0.555
UDF0960	0.681	0.486	0.700	0.505	0.682	0.452	0.755	0.562
UDF0971	0.641	0.503	0.646	0.493	0.677	0.536	0.714	0.566
UDF0982	0.603	0.355	0.616	0.428	0.611	0.349	0.699	0.545
DGs								
UDF0015	0.532	0.357	0.566	0.399	0.483	0.298	0.580	0.348
UDF0033	0.503	0.329	0.443	0.225	0.417	0.262	0.567	0.409
UDF0091	0.366	0.171	0.375	0.193	0.441	0.248	0.556	0.349
UDF0093	0.555	0.413	0.585	0.422	0.581	0.378	0.689	0.533
UDF0100	0.515	0.307	0.542	0.340	0.432	0.255	0.518	0.336
UDF0234	0.455	0.325	0.435	0.277	0.410	0.276	0.525	0.297
UDF0245	0.550	0.368	0.581	0.346	0.559	0.366	0.653	0.440
UDF0295	0.399	0.214	0.490	0.209	0.426	0.210	0.516	0.311
UDF0332	0.412	0.179	0.295	0.131	0.303	0.202	0.445	0.239
UDF0410	0.544	0.306	0.502	0.324	0.577	0.394	0.638	0.481
UDF0565	0.470	0.208	0.494	0.285	0.487	0.311	0.558	0.353
UDF0629	0.577	0.383	0.587	0.396	0.542	0.428	0.635	0.501
UDF0702	0.426	0.231	0.450	0.229	0.545	0.374	0.581	0.347
UDF0739	0.318	0.137	0.445	0.269	0.545	0.346	0.636	0.425
UDF1301	0.579	0.308	0.542	0.289	0.492	0.253	0.662	0.517
UDF1361	0.701	0.569	0.647	0.475	0.650	0.502	0.741	0.635
Mean-OGs	0.645	0.485	0.654	0.489	0.639	0.466	0.686	0.533
Mean-DGs	0.494	0.300	0.499	0.301	0.493	0.319	0.594	0.408

in Table 2. Column (1) lists the galaxy name. Columns (2) – (9) list the morphological parameters of *G* and *C*, using the HST *i*-, *z*-, *J*-, and *H*-band images. The mean values of these morphological parameters are listed in the last two rows of Table 2 for OGs and DGs, respectively.

Figure 9 shows the distribution of EROs in the log *G* versus log *C* plane. The EROs classified as OGs in the previous section are shown as red, DGs as blue. Firstly, a strong correlation between the Gini coefficient and the concentration index can be found for $z \sim 1$ EROs, as found by Abraham et al. (2003) for local galaxies. The correlation between *C* and *G* exists because highly concentrated galaxies have much of their light in a small number of pixels, then have high *G* values. Secondly, OGs have higher *G* and *C* values than DGs. This is what we have expected, since DGs are known to contain star formation and asymmetries produced by star formation or merging and tidal interactions with other galaxies. These galaxies thus have lower central concentration. Finally, we can find that the morphological parameters of galaxies in our sample depend on the wavelength of observation, from Figure 9 and Table 2. To show this point more clearly, we plot the mean values of *G* and *C* (pluses) for both OGs and DGs at each band as in Figure 9, and list the mean values in the last two rows of Table 2. For the same spatial resolution imaging data sets, galaxies have higher *G* and *C* when these morphological parameters are measured at longer wavelength bands, the similar findings can also be found in Abraham et al. (2003). Therefore, when studying the morphological evolution of galaxies as a function of redshift, morphological parameters should be measured with the same (or similar) rest-frame wavelength images.

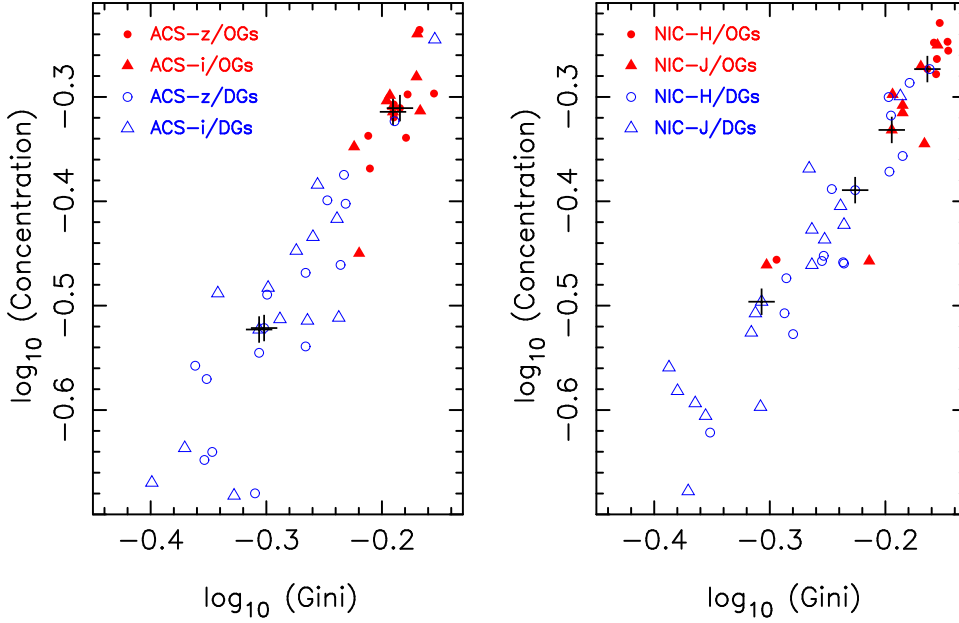


Fig. 9 Gini coefficient versus concentration index for EROs in the UDF. Left panel shows morphological parameters of HST/ACS i - and z -band, which have spatial resolution at $0.03'' \text{ pixel}^{-1}$; Right panel shows morphological parameters of HST/NICMOS J - and H -band, which have spatial resolution at $0.09'' \text{ pixel}^{-1}$. OGs are shown as red symbols, and DGs as blue. The mean values for DGs and OGs in different bands are shown as pluses.

5 SUMMARY

We have described the construction of a sample of extremely red objects within the Hubble Ultra Deep Field images, and developed four different methods for their classification. Taking advantage of the high-resolution HST/ACS and HST/NICMOS imaging, we also analyzed morphological parameters of galaxies while considering wavelength. Our main conclusions are as follows:

(1) We identify a sample of 24 EROs, defined here as $(i - K) > 3.9$ galaxies, to a limit $K_{\text{Vega}} = 22$ in the Hubble Ultra Deep Field. Compared to OGs, we find that most of the DGs are in the range of faint magnitude, while the fraction of OGs is similar to that of DGs to $K_{\text{Vega}} \leq 20.5$.

(2) To classify EROs in our sample, we develop four different methods, the SED fitting, $(i - K)$ vs. $(J - K)$ color, MIPS $24 \mu\text{m}$ image, and nonparametric measures of galaxy morphology. We found that the classification results from these methods agree well.

(3) Combining these methods, we separate OGs and DGs in our EROs sample. About 33% and 67% of them are classified as OGs and DGs, respectively.

(4) We measure the morphological parameters of G and C for the 24 EROs in the HST/ACS i -, z - ($0.03'' \text{ pixel}^{-1}$) and HST/NICMOS J -, H -band ($0.09'' \text{ pixel}^{-1}$) images in the UDF, respectively. For the same spatial resolution data sets, the results show that both OGs and DGs have lower G and C values at shorter wavelength bands. Furthermore, the strong correlation between the Gini coefficient and the concentration index of galaxies can be found at each band.

Considering that our EROs sample is small, we plan to use these classification methods to much larger fields, such as GOODS, GEMS and COSMOS, etc, examining the efficiency of these methods and studying the classification and physical properties of EROs in the future.

Acknowledgements We would like to thank Simon D. M. White and Emanuele Daddi for their valuable suggestions. We are grateful to Robert G. Abraham and Christopher J. Conselice for their comments and ac-

cess to their morphology analysis codes. The work is supported by the National Natural Science Foundation of China (NSFC, Nos. 10573014, 10633020, and 10873012), the Knowledge Innovation Program of the Chinese Academy of Science (No. KJCX2-YW-T05), and National Basic Research Program of China (973 Program) (No. 2007CB815404).

References

- Abraham R. G, Tanvir N. R, Santiago B. X. et al; 1996, MNRAS, 279, L47
- Abraham R. G, van den Bergh S, Nair P; 2003, ApJ, 588, 218
- Beckwith S. V. W, Stiavelli M, Koekemoer A. M. et al; 2006, AJ, 132, 1729
- Bershady M. A, Jangren A, Conselice C. J; 2000, AJ, 119, 2645
- Bertin E, Arnouts S; 1996, A&AS, 117, 393
- Bolzonella M, Miralles J.-M, Pelló R; 2000, A&A, 363, 476
- Broadhurst T. J, Ellis R. S, Glazebrook K; 1992, Nature, 335, 55
- Brown M. J. I, Jannuzi B. T, Dey A. et al; 2005, ApJ, 621, 41
- Capak P, Abraham R. G, Ellis R. S. et al; 2007, ApJS, 172, 284
- Calzetti D, Armus L, Bohlin R. C. et al; 2000, ApJ, 533, 682
- Cimatti A, Daddi E, Cassata P. et al; 2003, A&A, 412, L1
- Coe D, Benítez N, Sánchez S. F. et al; 2006, AJ, 132, 926
- Conselice C. J; 2003, ApJS, 147, 1
- Conselice C. J, Bundy K, U Vivian. et al; 2008a, MNRAS, 383, 1366
- Conselice C. J, Rajgor S, Myers R. 2008b, MNRAS, 386, 909
- Díaz-Sánchez A, Villo-Pérez I, Pérez-Garrido A. et al; 2007, MNRAS, 377, 516
- Elston R, Rieke G. H, Rieke M. J; 1988, ApJ, 331, 77
- Elston R, Rieke M. J, Rieke G. H; 1989, ApJ, 341, 80
- Furusawa H, Shimasaku K, Doi M. et al; 2000, ApJ, 534, 624
- Georgakakis A, Hopkins A. M, Afonso J. et al; 2006, MNRAS, 367, 331
- Giavalisco M, Ferguson H. C, Koekemoer A. M. et al; 2004, ApJ, 600, L93
- Hu E. M, Ridgway S. E; 1994, AJ, 107, 1303
- Kauffmann G, Charlot S; 1998, MNRAS, 297, L23
- Kitzbichler M. G, White S. D. M; 2007, MNRAS, 376, 2
- Kodama T, Arimoto N; 1997, A&A, 320, 41
- Kodama T, Bell E. F, Bower R. G. et al; 1999, MNRAS, 302, 152
- Kong X, Daddi E, Arimoto N. et al; 2006, ApJ, 638, 72
- Kong X, Zhang W, Wang M; 2008a, ChJAA, 1, 1
- Kong X, Fang G. W, Arimoto N, et al; 2008b, ApJ, submitted to ApJ
- Li H.-N, Wu H, Cao C, Zhu Y.-N; 2007, AJ, 134, 1315
- Lotz J. M, Primack J, Madau P; 2004, AJ, 128, 163
- Lotz, J. M, Davis M, Faber S. M. et al; 2008, ApJ, 672, 177
- Mannucci F, Pozzetti L, Thompson D. et al; 2002, MNRAS, 329, L57
- Miyazaki M, Shimasaku K, Kodama T. et al; 2003, PASJ, 55, 1079
- Moriondo G, Cimatti A, Daddi E; 2000, A&A, 364, 26
- Moustakas L. A, Casertano S, Conselice C. J. et al; 2004, ApJ, 600, L131
- Pozzetti L, Mannucci F; 2000, MNRAS, 317, L17
- Rieke G. H, Young E. T, Engelbracht C. W. et al; 2004, ApJS, 154, 25
- Rix H.-W, Barden M, Beckwith S. V. W. et al; 2004, ApJS, 152, 163
- Sawicki M, Stevenson M, Barrientos L. F. et al; 2005 ApJ, 627, 621

- Scodeggio M, Silva D. R; 2000, A&A, 359, 953
Scoville N, Aussel H, Brusa M. et al; 2007, ApJS, 172, 1
Shi Y, Rieke G. H, Papovich C. et al; 2006, ApJ, 645, 199
Simpson C, Almaini O, Cirasuolo M. et al; 2006, MNRAS, 373, 21
Smail I, Owen F. N, Morrison G. E. et al; 2002, ApJ, 581, 844
Stern D, Chary R.-R, Eisenhardt P. R. M. et al; 2006, AJ, 132, 1405
Stutz A. M, Papovich C, Eisenstein D. J. et al; 2008, ApJ, in press
Thompson R. I, Illingworth G, Bouwens R. et al; 2005, AJ, 130, 1
Werner M. W, Roellig T. L, Low F. J. et al; 2004, ApJS, 154, 1
Wilson G, Huang J.-S, Fazio G. G. et al; 2007, ApJ, 660, L59
Yan L, Thompson D; 2003, ApJ, 586, 765
Yan L, Choi P. I, Fadda D. et al; 2004, ApJS, 154, 75